

Two-dimensional topological superconductivity candidate in van der Waals layered material

Jing-Yang You,¹ Bo Gu,² Gang Su,² and Yuan Ping Feng^{1,3,*}

¹*Department of Physics, National University of Singapore, 2 Science Drive 3, Singapore 117551*

²*Kavli Institute for Theoretical Sciences, and CAS Center for Excellence in Topological Quantum Computation, University of Chinese Academy of Sciences, Beijing 100190, China*

³*Centre for Advanced 2D Materials, National University of Singapore, 6 Science Drive 2, Singapore 117546*

Two-dimensional (2D) topological superconductors are highly desired because they not only offer opportunities for exploring novel exotic quantum physics, but also possess potential applications in quantum computation. However, there are few reports about 2D superconductors, let alone topological superconductors. Here, we find a 2D monolayer W_2N_3 , which can be exfoliated from its real van der Waals bulk material with much lower exfoliation energy than MoS_2 , to be a topological metal with exotic topological states at different energy levels. Owing to the Van Hove singularities, the density of states near Fermi level are high, making the monolayer a compensate metal. Moreover, the monolayer W_2N_3 is unveiled to be a superconductor with the superconducting transition temperature $T_c \sim 22$ K and a superconducting gap of about 5 meV based on the anisotropic Migdal-Eliashberg formalism, arising from the strong electron-phonon coupling around the Γ point, and the 2D superconductor is phonon-mediated and fits the BCS mechanism with Ising-type pairing. Because of the strong electron and lattice coupling, the monolayer displays a non-Fermi liquid behavior in its normal states at temperatures lower than 80 K, where the specific heat exhibit T^3 behavior and the Wiedemann-Franz law dramatically violates. Our findings not only provide the platform to study the emergent phenomena in 2D topological superconductors, but also open a door to discover more 2D high-temperature topological superconductors in van der Waals materials.

Introduction—Two-dimensional (2D) materials have been extensively studied due to their intriguing properties, such as magnetism^{1–4}, topological states^{5–7}, superconductivity^{8–10} and so on. Since the successful exfoliation of graphene in 2004¹¹, several 2D materials including MoS_2 ^{12,13}, CrI_3 ¹, $CrGeTe_3$ ², etc., have been synthesized in experiments. Among these 2D materials, single atomic layer materials are particularly fascinating because they can be easily exfoliated from their van der Waals bulk materials and can be constructed into multifarious heterostructures to realize composite and extraordinary physical phenomena^{14–19}.

2D superconductors exfoliated from van der Waals bulk materials represent a unique class of 2D superconductivity because of the easy fabrication and the absence of the substrate^{20–27}. While the exotic properties related to them, the discovery of these exfoliated 2D superconductors has been rarely reported. The monolayer transition metal dichalcogenides, $NbSe_2$, TaS_2 and $TiSe_2$ display coexisting superconductivity and charge density wave driven by electron-phonon coupling^{10,22,27–33}. Recently, the monolayer $NiTe_2$ was reported to be a two-gap superconductivity with a $T_c \sim 5.7$ K, and the T_c can be enhanced to 11.3 K by inserting one lithium atomic layer into bilayer $NiTe_2$ ³⁴. These 2D superconductors provide great opportunities for exploring fascinating quantum physics. The discovery of 2D topological materials, such as quantum spin Hall^{5,6}, quantum anomalous Hall insulators⁷ and topological (semi-) metals^{35–37}, sheds insightful light on the study of emerging physical phenomena because of the interplay of superconductivity and nontrivial topology. The emergent topological superconductors with Majorana fermions are thought to be useful for

fault-tolerant quantum computation^{38–40}. Topological superconductivity was proposed to be induced in topological boundary states of heterostructures composed of topological materials and superconductors by proximity effects^{38–40}. However, the interface conditions dramatically influence the observation of topological superconductivity. Therefore, discovering 2D materials with simultaneously superconductivity and nontrivial topology will be of great value to achieve topological superconductivity. Although several 2D superconductors have been obtained, very few of them can exhibit topological states^{41–46}. Thus, a crucial issue is to fabricate novel 2D materials with simultaneously superconductivity and nontrivial topology, where van der Waals materials may play an important role.

In this work, we report a detail investigation of the superconductivity and nontrivial electronic topology in 2D monolayer W_2N_3 ⁴⁷. The monolayer W_2N_3 exhibits a topological metal with three nodal lines traversing the whole Brillouin zone (BZ), which are protected by the symmetries. Topological surface states with respect to these nontrivial band topology are also investigated. Moreover, the monolayer W_2N_3 is found to be a superconductor with the superconducting transition temperature of about 22 K and the superconducting gap up to 5 meV based on the anisotropic Migdal-Eliashberg formalism. This 2D superconductor is phonon-mediated and fits the BCS mechanism with Ising-type pairing. The high T_c and large superconducting gap are revealed to result from the enhanced electron-phonon coupling (EPC) near Fermi level at Γ point. The strong electron-phonon coupling come from the high density of states near Fermi level brought about by the Van Hove singularities near

Fermi level, leading to more electrons susceptible to pairing mediated by phonons. Besides, owing to the strong electron-phonon coupling, the normal states of monolayer W_2N_3 perform as a non-Fermi liquid at temperatures lower than 80 K, where the electrical specific heat shows a cubic dependence of temperature and the Wiedemann-Franz law is obviously violated. The coexistence of superconductivity and nontrivial band topology in this layered material makes it an inevitable platform to study topological superconductivity.

Calculation Method—Our first-principles calculations were based on the density functional theory (DFT) as implemented in the QUANTUM ESPRESSO package⁴⁸, using the full relativistic pseudopotential. The vacuum layer was set to 15 Å. To warrant an energy convergence of less than 1 meV per atom, the plane waves kinetic-energy cutoff was set as 100 Ry and the energy cutoff for charge density was set as 1250 Ry. The structural optimization was performed until the forces on atoms were less than 1 meV/Å. An unshifted BZ \mathbf{k} point mesh of $20 \times 20 \times 1$ was utilized for electronic charge density calculations. The phonon modes are computed within density-functional perturbation theory¹⁶ on a $10 \times 10 \times 1$ \mathbf{q} mesh. The EPW code^{49–51} was employed for the calculation of superconducting gap with both fine \mathbf{k} and \mathbf{q} meshes of $100 \times 100 \times 1$ in the BZ. The surface spectrum was calculated by using the Wannier functions and the iterative Green’s function method^{52–55}. The electronic and phonon transport properties were calculated with the packages BoltzTrap⁵⁶ and ShengBTE⁵⁷, respectively.

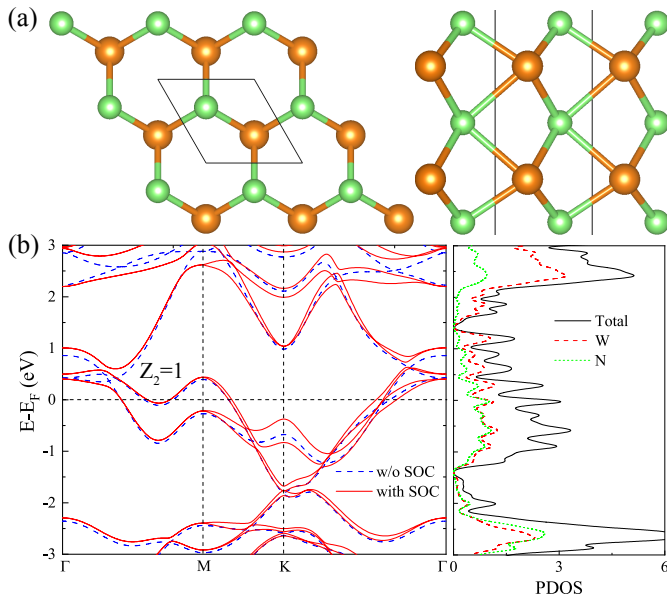


FIG. 1. (a) Top and side views of the crystalline structure of monolayer W_2N_3 . (b) Electronic band structures of monolayer W_2N_3 without (dash blue lines) and with (solid red lines) SOC, and the corresponding partial density of states (DOS) with SOC. The Brillouin zone (BZ) with high symmetry paths is inserted.

Crystal structure—The bulk W_2N_3 has a van der Waals layered crystal structure with the space group of $P6_3/mmc$ (No.194)⁵⁸. It is composed of inversion symmetric N-W-N-W-N layers with two 1T N-W-N layers sharing one layer of N atoms as shown in Fig. 1(a), and shows AB stacking along the (0001) direction. The monolayer W_2N_3 with the space group of $P\bar{6}m2$ (No.187) can be easily exfoliated from its bulk material due to the low exfoliation energy of 46.6 meV/atom^{47,59}, which is much lower than that for monolayer MoS_2 with 76.3 meV/atom⁶⁰. The in-plane lattice constant of monolayer W_2N_3 is optimized to be $a = 2.864$ Å, which is reasonable compared with the in-plane lattice constant of its bulk⁵⁸.

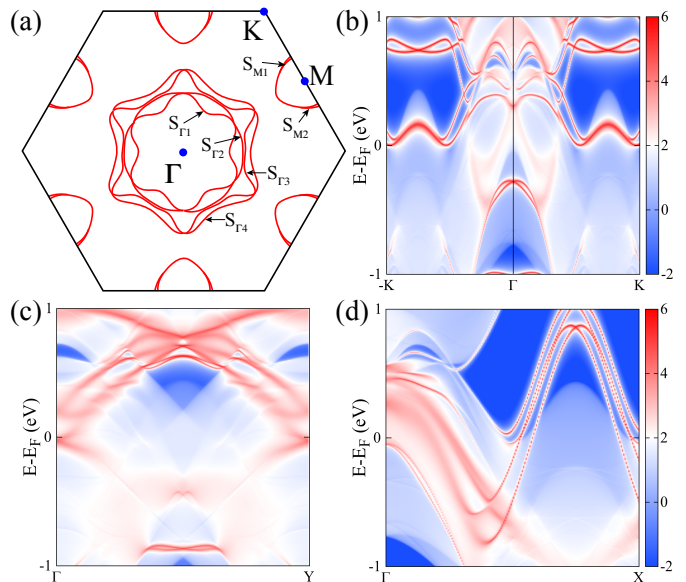


FIG. 2. (a) Fermi surfaces (red lines) for monolayer W_2N_3 . The surface states of monolayer W_2N_3 projected on (b) (111), (c) (100) and (d) (010) planes, respectively. Warmer colors represent higher local density of states, and blue regions indicate the bulk band gap.

Topological states—The electronic structure of monolayer W_2N_3 without and with spin-orbital coupling (SOC) as well as the partial DOS with SOC are plotted in Fig. 1(b). By comparing the electronic band structures of monolayer W_2N_3 without and with SOC, one may observe that the SOC removes some degenerate points and significantly changes the band structure because of the heavy W atoms possessing relative large SOC. Thus, all results discussed in the following were calculated with SOC included. For monolayer W_2N_3 , there are four bands crossing the Fermi level, making the monolayer a compensated metal as shown in Fig. 1(b). There are three flower-shaped hole pockets (labeled as $S_{\Gamma_{1,2,3}}$, from the inside out) and one electron pocket (S_{Γ_4}) at Γ point. At the centers of the boundary of BZ, M, are elliptical hole (S_{M_1}) and electron (S_{M_2}) pockets [Fig. 2(a)]. The W and N atoms contribute almost equally to the low energy band structure and DOS near Fermi level because of

the large p - d hybridization. The band structures present many interesting features: the SOC lifts the degenerate points at 0.5 eV above Fermi level, leading to the nontrivial band topology characterized by the topological invariant $Z_2 = 1$; both without and with SOC the Weyl points at about 1.5 eV below Fermi level at K (K') points are stable, which are protected by the symmetries at K (K') points; it is interesting to note that the two-fold band degeneracy along the high symmetry lines Γ -M exists both without and with SOC; there are several Van Hove singularities in the band structure leading to sharp peaks of DOS, in particularly the Van Hove singularities at about 0.1 eV below Fermi level bringing about high DOS near Fermi level. The two-fold degeneracy along Γ -M high symmetry lines is protected by the symmetries, because when SOC is included any point on Γ -M lines belongs to the group G_8^5 with the reality of a , which only possesses two-dimensional irreducible representation⁶¹, constraining the two-fold degeneracy along Γ -M at all energy scale. These nontrivial topological states are fully reflected in their surface states as shown in Figs. 2(b), (c) and (d), where abundant topological surface states can be seen.

Superconductivity—The metallic property with high DOS near Fermi level motivated us to investigate the possible superconductivity. The phonon spectra, the phonon density of states (PhDOS), the Eliashberg electron-phonon spectral function $\alpha^2F(\omega)$ and the cumulative frequency dependent EPC $\lambda(\omega)$ are shown in Fig. 3(a). The absence of imaginary frequency modes indicates the dynamical stability of monolayer W_2N_3 as shown in Fig. 3(a). From the projected PhDOS, we find that W atoms vibrate in the low frequency region, while N atoms vibrate in the relative higher frequency region because their distinct atomic masses, and the phonon vibrational modes of W and N atoms are separated by a phonon spectral energy gap of about 6 meV. $\alpha^2F(\omega)$ displays a dominant peak centered around 10 meV at the low frequency region, while $\alpha^2F(\omega)$ is more spread at the high frequency region. The cumulative frequency-dependent EPC $\lambda(\omega)$ can be calculated by integrating $\alpha^2F(\omega)$. From the calculated $\lambda(\omega)$, we find that the low-frequency phonons (below the phonon spectral gap (35 meV)) account for 74% of the total EPC [$\lambda = \lambda(\infty) = 1.47$]. Thus, W atoms make the main contribution to the EPC. Utilizing our calculated $\alpha^2F(\omega)$ and $\lambda(\omega)$ together with a typical value of the effective screened Coulomb repulsion constant $\mu^* = 0.1$, the superconducting transition temperature T_c is calculated to be 21 K with the McMillan-Allen-Dynes (MAD) approach^{62–64}, which is highest reported for 2D superconductors exfoliated from van der Waals bulk materials.

Figure 3(b) shows the quasiparticle DOS in the superconducting state at two representative temperatures of 6 and 18 K, relative to the DOS in the normal state as a function of frequency ω (meV) based on the anisotropic Migdal-Eliashberg theory^{49–51}. We can observe that the superconducting gaps at 6 and 18 K are about 5 and 4 meV, respectively. The k -resolved superconducting gaps

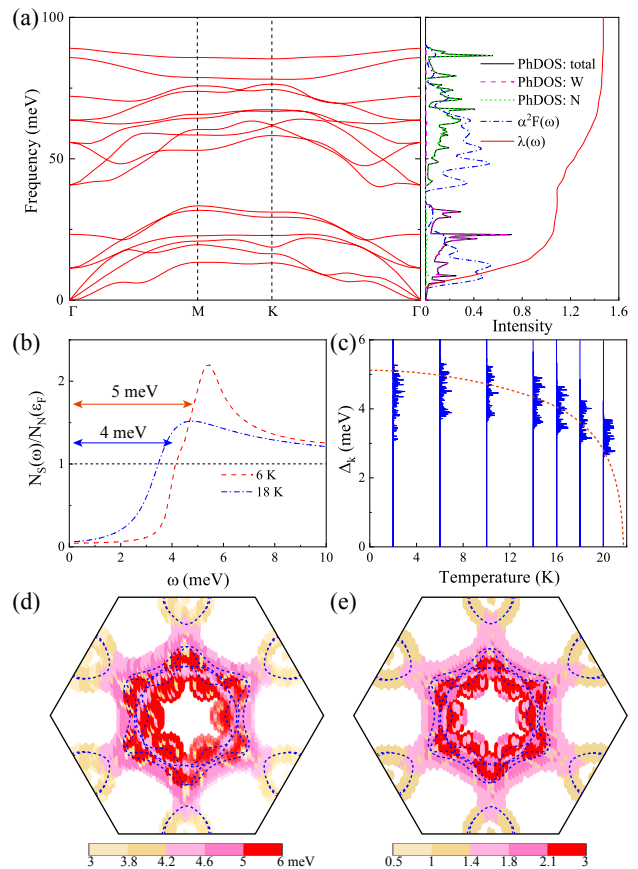


FIG. 3. (a) The phonon spectrum and phonon density of states (PhDOS) (multiply 5), Eliashberg spectral function $\alpha^2F(\omega)$, and the cumulative frequency-dependent of EPC $\lambda(\omega)$ of monolayer W_2N_3 at ambient pressure. (b) Quasiparticle DOS in the superconducting state for two representative temperatures of 6 K (red dashed line) and 18 K (blue dash-dotted line). The black dashed line indicates the DOS of normal state, which is normalized to 1 at the Fermi level. The superconducting DOS $N_S(\omega)$ becomes 1 beyond the highest phonon energy. (c) Anisotropic superconducting gap of monolayer W_2N_3 on the Fermi surface as a function of temperature. Red dashed curve is BCS fit of the superconducting gap. (d) Momentum-resolved superconducting gap Δ_k on the Fermi surface (blue dashed lines) at 10 K, where warmer color (red) indicates bigger Δ_k . (e) Momentum-resolved electron-phonon coupling strength λ_k within 0.2 eV on the Fermi surface (blue dashed curves). Warmer colors (dark red) indicates larger λ_k .

on the Fermi surface, $\Delta_k(T)$, for several temperatures below 20 K with $\omega=0$, as well as the BCS fit for the superconducting gap are display in Fig. 3(c). It is seen that the superconducting gap vanishes at around 21.7 K, which is a little higher than the T_c (21 K) obtained with McMillan-Allen-Dynes (MAD) approach, and the zero-temperature superconducting gap is about 5 meV.

Figure 3(d) shows the momentum-resolved superconducting gap on the Fermi surface. On the whole Fermi surface, there are finite superconducting gaps, indicating the Fermi surface is fully gapped below T_c . The

superconducting gap on the S_{Γ_1} line exhibits larger gap distribution around the lowland on Γ -K paths, while the largest superconducting gaps on the S_{Γ_3} and S_{Γ_4} lines distribute on Γ -M paths, and the superconducting gap on the S_{Γ_2} line is smaller than that on the above three Fermi surface lines. The superconducting gaps on the S_{M_1} and S_{M_2} lines is about 2 meV smaller than that on the S_{Γ} lines. It is noted that the superconducting gaps both on the S_{Γ} and S_M lines are highly anisotropic. The regions of the Fermi surface with the largest superconducting gap coincide with the electron-phonon coupling strength λ_k as shown in Fig. 3(e). Thus, the high T_c and large Δ_k in monolayer W_2N_3 are mainly from the strong electron-phonon coupling of Fermi surface at Γ point.

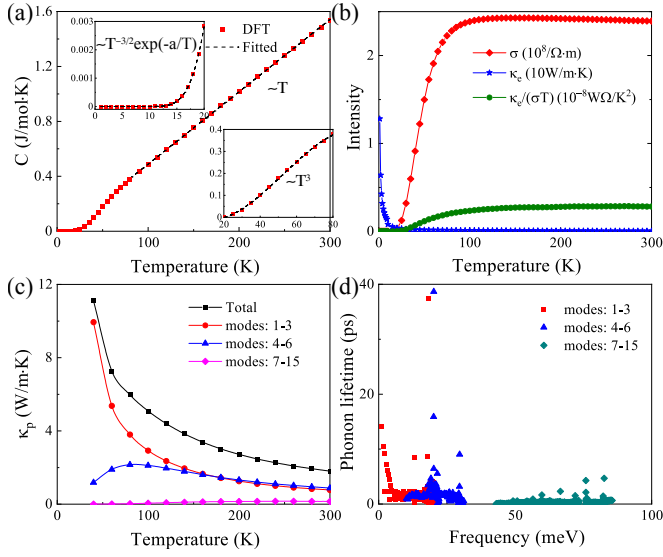


FIG. 4. (a) Temperature dependence of electronic specific heat C of monolayer W_2N_3 . The upper and lower insets are the enlarged parts of the specific heat at temperatures below T_c ($T < 20$ K), and above T_c ($20 < T < 80$ K), respectively. The black dashed lines are fitting curves at different temperature regions. (b) Temperature dependent electrical (σ) and thermal (κ_e) conductivities, and Lorenz number L [$L = \kappa_e/(\sigma T)$]. (c) The modes-resolved lattice thermal conductivity κ_p as a function of temperature. (d) The modes-resolved phonon lifetime as a function of frequency at 300 K.

Transport properties—It is worth mentioning that due to the exceedingly strong coupling between the electrons and phonons, the normal state of monolayer W_2N_3 may be a non-Fermi liquid. The temperature dependent electronic specific heat of monolayer W_2N_3 is calculated as shown in Fig. 4(a). It is noted that the specific heat $C(T)$ displays distinct features: at low temperature (below T_c), $C(T) \sim T^{-3/2} \cdot \exp(-a/T)$, i.e. the specific heat accords with the low-temperature specific heat of BCS superconductors (upper inset); at $20 < T < 80$ K, $C(T) \sim T^3$ (lower inset); and at high temperature region ($T > 80$ K), $C(T) \sim T$. It is clear that below 80 K, the normal state shows a non-Fermi liquid behavior⁶⁵.

To further verify this observation, the temperature dependent Lorenz number $L [= \kappa_e/(\sigma T)]$ is also studied, as presented in Fig. 4(b). We can observe that the Lorenz number L is not a constant at temperature below 80 K, which dramatically violates the Wiedemann-Franz law⁶⁶, while at high temperature it shows almost a constant, indicating a Fermi liquid behavior.

The lattice thermal conductivity is given in Fig. 4(c). It can be observed at temperatures lower than 200 K, the lattice thermal conductivity dominates, while at temperatures above 200 K, the electrical thermal conductivity dominates. It is noted that at low temperatures, the three acoustic modes (modes: 1-3) make the main contribution to lattice thermal conductivity, while with the increase of temperature the contribution of three optical branches from the vibration of N atoms (modes: 4-6) begins to match or even surpass that of the acoustic branches. The optical branches from vibration of N atoms (modes: 7-15) make little contribution to the thermal conductivity at the whole temperature range.

To gain more insight into phonon transport of monolayer W_2N_3 , the modes-resolved phonon lifetime is plotted in Fig. 4(d). It is found that most of phonon lifetimes of three acoustic branches are comparable with three optical branches from W atoms vibration, showing a comparable contribution to the lattice thermal conductivity, while the phonon lifetime of the optical branches above 40 meV is shorter because of the larger scattering rate. Thus, the N atoms contribute little to the thermal conductivity, leading to the low thermal conductivity of monolayer W_2N_3 .

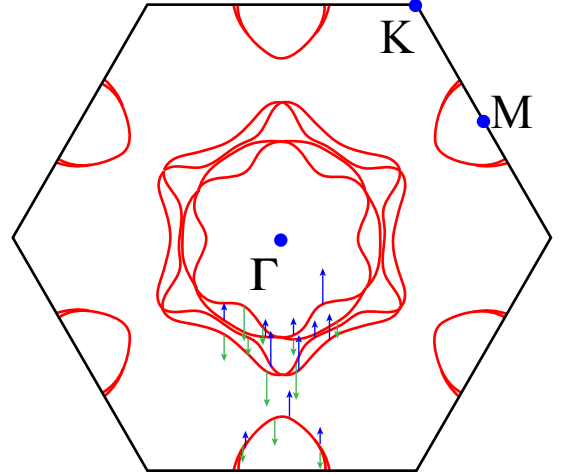


FIG. 5. Spin texture of electronic bands that cross the Fermi level, where the up (blue) and down (green) arrows represent the opposite out-of-plane spin polarization directions. In this figure we only plot the spin texture of partial Fermi surface, and the spin texture in other parts of the Fermi surface can be obtained by symmetries.

Discussion—To unveil the pairing mechanism and possible relation between the nontrivial band topology and superconductivity, the spin texture of Fermi surface is

calculated as plotted in Fig. 5. From Fig. 5(a), it is noted that each Fermi line is fully out-of-plane spin polarized, indicating an Ising-type pairing in monolayer W_2N_3 . This result is similar to the superconductivity in ion-gated MoS_2 ⁸. However, the magnitude of spin moments is different at different \mathbf{k} points on Fermi surface for monolayer W_2N_3 . The spin polarization direction between the outer and inner Fermi surface is inverted at the degenerate points on $\Gamma - M$ paths, at which the spin up and spin down are cancelled. Comparing the Figs. 3(d) and 5, it is interesting to note that the strength of electron-phonon coupling is related to the magnitude of spin moment, that is to say, where the magnitude of spin moment is large, the electron-phonon coupling is also enhanced. Since the superconductivity is related to the degeneracy point, which determines the topological metal state of monolayer W_2N_3 , there may be some correlation between the topology and superconductivity in our system, which needs further deep-going study.

Summary—In this work, we report that a 2D monolayer W_2N_3 hosts simultaneously topological states and superconductivity. The monolayer is found to exhibit different topological states at different energy level including topological Z_2 insulator, Weyl semimetal and topological nodal lines metal. The exotic topological

surface states are also investigated. Furthermore, based on anisotropic Migdal-Eliashberg theory, the monolayer W_2N_3 is predicted to be a phonon-mediated BCS superconductor with the superconducting transition temperature $T_c \sim 22$ K and the superconducting gap $\Delta_k \sim 5$ meV. The high T_c and large Δ_k are unveiled to be from the enhanced electron and lattice coupling near Fermi level at Γ point. Due to the large electron-phonon coupling, the normal state of monolayer W_2N_3 performs as a non-Fermi liquid at temperatures below 80 K, where the electrical specific heat displays a T^3 behavior and the Wiedemann-Franz law is dramatically violated. Our results will spur the observation of 2D high-temperature topological superconductivity.

ACKNOWLEDGEMENT

This research/project is supported by the Ministry of Education, Singapore, under its MOE AcRF Tier 3 Award MOE2018-T3-1-002. B.G. and G.S. are supported in part by the National Key R&D Program of China (Grant No. 2018YFA0305800), the Strategic Priority Research Program of the Chinese Academy of Sciences (Grant No. XDB28000000), and NSFC (Grant No.11834014).

* phyfyp@nus.edu.sg

- ¹ B. Huang, G. Clark, E. Navarro-Moratalla, D. R. Klein, R. Cheng, K. L. Seyler, D. Zhong, E. Schmidgall, M. A. McGuire, D. H. Cobden, W. Yao, D. Xiao, P. Jarillo-Herrero, and X. Xu, *Nature* **546**, 270 (2017).
- ² C. Gong, L. Li, Z. Li, H. Ji, A. Stern, Y. Xia, T. Cao, W. Bao, C. Wang, Y. Wang, Z. Q. Qiu, R. J. Cava, S. G. Louie, J. Xia, and X. Zhang, *Nature* **546**, 265 (2017).
- ³ Y. Deng, Y. Yu, Y. Song, J. Zhang, N. Z. Wang, Z. Sun, Y. Yi, Y. Z. Wu, S. Wu, J. Zhu, J. Wang, X. H. Chen, and Y. Zhang, *Nature* **563**, 94 (2018).
- ⁴ D. J. O'Hara, T. Zhu, A. H. Trout, A. S. Ahmed, Y. K. Luo, C. H. Lee, M. R. Brenner, S. Rajan, J. A. Gupta, D. W. McComb, and R. K. Kawakami, *Nano Lett.* **18**, 3125 (2018).
- ⁵ B. A. Bernevig, T. L. Hughes, and S.-C. Zhang, *Science* **314**, 1757 (2006).
- ⁶ M. König, S. Wiedmann, C. Brune, A. Roth, H. Buhmann, L. W. Molenkamp, X.-L. Qi, and S.-C. Zhang, *Science* **318**, 766 (2007).
- ⁷ C.-Z. Chang, J. Zhang, X. Feng, J. Shen, Z. Zhang, M. Guo, K. Li, Y. Ou, P. Wei, L.-L. Wang, Z.-Q. Ji, Y. Feng, S. Ji, X. Chen, J. Jia, X. Dai, Z. Fang, S.-C. Zhang, K. He, Y. Wang, L. Lu, X.-C. Ma, and Q.-K. Xue, *Science* **340**, 167 (2013).
- ⁸ Y. Saito, Y. Nakamura, M. S. Bahramy, Y. Kohama, J. Ye, Y. Kasahara, Y. Nakagawa, M. Onga, M. Tokunaga, T. Nojima, Y. Yanase, and Y. Iwasa, *Nat. Phys.* **12**, 144 (2015).
- ⁹ J. M. Lu, O. Zheliuk, I. Leermakers, N. F. Q. Yuan, U. Zeitler, K. T. Law, and J. T. Ye, *Science* **350**, 1353 (2015).
- ¹⁰ X. Xi, Z. Wang, W. Zhao, J.-H. Park, K. T. Law, H. Berger, L. Forró, J. Shan, and K. F. Mak, *Nat. Phys.* **12**, 139 (2015).
- ¹¹ K. S. Novoselov, *Science* **306**, 666 (2004).
- ¹² A. Splendiani, L. Sun, Y. Zhang, T. Li, J. Kim, C.-Y. Chim, G. Galli, and F. Wang, *Nano Lett.* **10**, 1271 (2010).
- ¹³ Y. Li, H. Wang, L. Xie, Y. Liang, G. Hong, and H. Dai, *J. Am. Chem. Soc.* **133**, 7296 (2011).
- ¹⁴ A. K. Geim and I. V. Grigorieva, *Nature* **499**, 419 (2013).
- ¹⁵ K. S. Novoselov, A. Mishchenko, A. Carvalho, and A. H. C. Neto, *Science* **353**, aac9439 (2016).
- ¹⁶ S. Baroni, S. de Gironcoli, A. D. Corso, and P. Giannozzi, *Rev. Mod. Phys.* **73**, 515 (2001).
- ¹⁷ M.-Y. Li, C.-H. Chen, Y. Shi, and L.-J. Li, *Mater. Today* **19**, 322 (2016).
- ¹⁸ J. Zhang, L. Du, S. Feng, R.-W. Zhang, B. Cao, C. Zou, Y. Chen, M. Liao, B. Zhang, S. A. Yang, G. Zhang, and T. Yu, *Nat. Commun.* **10**, 4226 (2019).
- ¹⁹ C. Gong, E. M. Kim, Y. Wang, G. Lee, and X. Zhang, *Nat. Commun.* **10**, 2657 (2019).
- ²⁰ Y. Saito, T. Nojima, and Y. Iwasa, *Nature Reviews Materials* **2**, 16094 (2016).
- ²¹ I. Guillaumon, H. Suderow, S. Vieira, L. Cario, P. Diener, and P. Rodière, *Phys. Rev. Lett.* **101**, 166407 (2008).
- ²² M. M. Ugeda, A. J. Bradley, Y. Zhang, S. Onishi, Y. Chen, W. Ruan, C. Ojeda-Aristizabal, H. Ryu, M. T. Edmonds, H.-Z. Tsai, A. Riss, S.-K. Mo, D. Lee, A. Zettl, Z. Hussain, Z.-X. Shen, and M. F. Crommie, *Nat. Phys.* **12**, 92 (2015).
- ²³ Y. Cao, V. Fatemi, S. Fang, K. Watanabe, T. Taniguchi, E. Kaxiras, and P. Jarillo-Herrero, *Nature* **556**, 43 (2018).

- ²⁴ D. Jiang, T. Hu, L. You, Q. Li, A. Li, H. Wang, G. Mu, Z. Chen, H. Zhang, G. Yu, J. Zhu, Q. Sun, C. Lin, H. Xiao, X. Xie, and M. Jiang, *Nat. Commun.* **5**, 5708 (2014).
- ²⁵ Y. Yu, L. Ma, P. Cai, R. Zhong, C. Ye, J. Shen, G. D. Gu, X. H. Chen, and Y. Zhang, *Nature* **575**, 156 (2019).
- ²⁶ X. Xi, L. Zhao, Z. Wang, H. Berger, L. Forró, J. Shan, and K. F. Mak, *Nat. Nanotechnol.* **10**, 765 (2015).
- ²⁷ E. Navarro-Moratalla, J. O. Island, S. Mañas-Valero, E. Pinilla-Cienfuegos, A. Castellanos-Gomez, J. Queda, G. Rubio-Bollinger, L. Chirulli, J. A. Silva-Guillén, N. Agrait, G. A. Steele, F. Guinea, H. S. J. van der Zant, and E. Coronado, *Nat. Commun.* **7**, 11043 (2016).
- ²⁸ T. Valla, A. V. Fedorov, P. D. Johnson, P.-A. Glans, C. McGuinness, K. E. Smith, E. Y. Andrei, and H. Berger, *Phys. Rev. Lett.* **92**, 086401 (2004).
- ²⁹ F. Zheng, Z. Zhou, X. Liu, and J. Feng, *Phys. Rev. B* **97**, 081101(R) (2018).
- ³⁰ F. Zheng and J. Feng, *Phys. Rev. B* **99**, 161119(R) (2019).
- ³¹ B. Sipoš, A. F. Kusmartseva, A. Akrap, H. Berger, L. Forró, and E. Tutiš, *Nat. Mater.* **7**, 960 (2008).
- ³² R. A. Klemm, *Physica C: Superconductivity and its Applications* **514**, 86 (2015).
- ³³ M. Calandra and F. Mauri, *Phys. Rev. Lett.* **106**, 196406 (2011).
- ³⁴ F. Zheng, X.-B. Li, P. Tan, Y. Lin, L. Xiong, X. Chen, and J. Feng, *Phys. Rev. B* **101**, 100505(R) (2020).
- ³⁵ A. A. Burkov, *Nat. Mater.* **15**, 1145 (2016).
- ³⁶ C.-K. Chiu, J. C.Y. Teo, A. P. Schnyder, and S. Ryu, *Rev. Mod. Phys.* **88**, 035005 (2016).
- ³⁷ A. Bansil, H. Lin, and T. Das, *Rev. Mod. Phys.* **88**, 021004 (2016).
- ³⁸ L. Fu and C. L. Kane, *Phys. Rev. Lett.* **100**, 096407 (2008).
- ³⁹ M. Z. Hasan and C. L. Kane, *Rev. Mod. Phys.* **82**, 3045 (2010).
- ⁴⁰ X.-L. Qi and S.-C. Zhang, *Rev. Mod. Phys.* **83**, 1057 (2011).
- ⁴¹ Y.-F. Lv, W.-L. Wang, Y.-M. Zhang, H. Ding, W. Li, L. Wang, K. He, C.-L. Song, X.-C. Ma, and Q.-K. Xue, *Science Bulletin* **62**, 852 (2017).
- ⁴² M. Liao, Y. Zang, Z. Guan, H. Li, Y. Gong, K. Zhu, X.-P. Hu, D. Zhang, Y. Xu, Y.-Y. Wang, K. He, X.-C. Ma, S.-C. Zhang, and Q.-K. Xue, *Nat. Phys.* **14**, 344 (2018).
- ⁴³ G. C. Ménard, S. Guissart, C. Brun, R. T. Leriche, M. Trif, F. Debontridder, D. Demaille, D. Roditchev, P. Simon, and T. Cren, *Nat. Commun.* **8**, 2040 (2017).
- ⁴⁴ F. Fei, X. Bo, R. Wang, B. Wu, J. Jiang, D. Fu, M. Gao, H. Zheng, Y. Chen, X. Wang, H. Bu, F. Song, X. Wan, B. Wang, and G. Wang, *Phys. Rev. B* **96**, 041201(R) (2017).
- ⁴⁵ H. Leng, C. Paulsen, Y. K. Huang, and A. de Visser, *Phys. Rev. B* **96**, 220506(R) (2017).
- ⁴⁶ C. Liu, C.-S. Lian, M.-H. Liao, Y. Wang, Y. Zhong, C. Ding, W. Li, C.-L. Song, K. He, X.-C. Ma, W. Duan, D. Zhang, Y. Xu, L. Wang, and Q.-K. Xue, *Physical Review Materials* **2**, 094001 (2018).
- ⁴⁷ H. Yu, X. Yang, X. Xiao, M. Chen, Q. Zhang, L. Huang, J. Wu, T. Li, S. Chen, L. Song, L. Gu, B. Y. Xia, G. Feng, J. Li, and J. Zhou, *Adv. Mater.* **30**, 1805655 (2018).
- ⁴⁸ P. Giannozzi, S. Baroni, N. Bonini, M. Calandra, R. Car, C. Cavazzoni, D. Ceresoli, G. L. Chiarotti, M. Cococcioni, I. Dabo, A. D. Corso, S. de Gironcoli, S. Fabris, G. Fratesi, R. Gebauer, U. Gerstmann, C. Gougoussis, A. Kokalj, M. Lazzeri, L. Martin-Samos, N. Marzari, F. Mauri, R. Mazzarello, S. Paolini, A. Pasquarello, L. Paulatto, C. Sbraccia, S. Scandolo, G. Sclauzero, A. P. Seitsonen, A. Smogunov, P. Umari, and R. M. Wentzcovitch, *J. Phys.: Condens. Matter* **21**, 395502 (2009).
- ⁴⁹ F. Giustino, M. L. Cohen, and S. G. Louie, *Phys. Rev. B* **76**, 165108 (2007).
- ⁵⁰ E. R. Margine and F. Giustino, *Phys. Rev. B* **87**, 024505 (2013).
- ⁵¹ S. Poncé, E. Margine, C. Verdi, and F. Giustino, *Comput. Phys. Commun.* **209**, 116 (2016).
- ⁵² N. Marzari and D. Vanderbilt, *Phys. Rev. B* **56**, 12847 (1997).
- ⁵³ I. Souza, N. Marzari, and D. Vanderbilt, *Phys. Rev. B* **65**, 035109 (2001).
- ⁵⁴ Q. Wu, S. Zhang, H.-F. Song, M. Troyer, and A. A. Soluyanov, *Comput. Phys. Commun.* **224**, 405 (2018).
- ⁵⁵ M. P. L. Sancho, J. M. L. Sancho, J. M. L. Sancho, and J. Rubio, *J. Phys. F: Met. Phys.* **15**, 851 (1985).
- ⁵⁶ G. K. Madsen and D. J. Singh, *Comput. Phys. Commun.* **175**, 67 (2006).
- ⁵⁷ W. Li, J. Carrete, N. A. Katcho, and N. Mingo, *Comput. Phys. Commun.* **185**, 1747 (2014).
- ⁵⁸ S. Wang, X. Yu, Z. Lin, R. Zhang, D. He, J. Qin, J. Zhu, J. Han, L. Wang, H. kwang Mao, J. Zhang, and Y. Zhao, *Chem. Mater.* **24**, 3023 (2012).
- ⁵⁹ N. Mounet, M. Gibertini, P. Schwaller, D. Campi, A. Merkys, A. Marrazzo, T. Sohier, I. E. Castelli, A. Cepellotti, G. Pizzi, and N. Marzari, *Nat. Nanotechnol.* **13**, 246 (2018).
- ⁶⁰ J. Zhou, L. Shen, M. D. Costa, K. A. Persson, S. P. Ong, P. Huck, Y. Lu, X. Ma, Y. Chen, H. Tang, and Y. P. Feng, *Sci. Data* **6**, 86 (2019).
- ⁶¹ H. Wondratschek, *Acta Crystallographica Section A* **29**, 581 (1973).
- ⁶² W. L. McMillan, *Phys. Rev.* **167**, 331 (1968).
- ⁶³ P. B. Allen and R. C. Dynes, *Phys. Rev. B* **12**, 905 (1975).
- ⁶⁴ F. Giustino, *Rev. Mod. Phys.* **89**, 015003 (2017).
- ⁶⁵ A. J. Schofield, *Contemp. Phys.* **40**, 95 (1999).
- ⁶⁶ R. Franz and G. Wiedemann, *Annalen der Physik und Chemie* **165**, 497 (1853).